Optimal Coordinated Control of Multi-Renewable-to-Hydrogen Production System for Hydrogen Fueling Stations

Kuan Zhang, Bin Zhou, *Senior Member*, *IEEE*, Siu Wing Or, Canbing Li, *Senior Member*, *IEEE*, Chi Yung Chung, *Fellow*, *IEEE*, Nikolai Voropai, *Life Fellow*, *IEEE*

[1]***Abstract*—Under the pressure of climate change, the demands for alternative green hydrogen (H_2) production methods have been on the rise to conform to the global trend of transition to a H_2 society. This paper proposes a multi-renewable-to-hydrogen production method to enhance the green H_2 production efficiency for renewable-dominated hydrogen fueling stations (HFSs). In this method, the aqueous electrolysis of native biomass can be powered by wind and solar generations based on electrochemical effects, and both electrolysis current and temperature are taken into account for facilitating on-site H_2 production and reducing the electricity consumption. Moreover, a capsule network (CN)-based H_2 demand forecasting model is formulated to estimate the gas load for HFS by extracting the underlying spatial features and temporal dependencies of traffic flows in the transportation network. Furthermore, a hierarchical coordinated control strategy is developed to suppress high fluctuations in electrolysis current caused by volatility of wind and solar outputs based on model predictive control (MPC) framework. Comparative studies validate the superior performance of the proposed methodology over the power-to-gas (P2G) scheme on electrolysis efficiency and economic benefits.**

***Index Terms*—Hybrid energy system, hydrogen, hydrogen filling station, hydrogen economy, energy management.**

I. Introduction

A. Motivation

Hydrogen-powered vehicles (HVs) have attracted worldwide attentions as green transportation due to their zero-emission, high mileage range and fast refueling features [1]. The proliferation of hydrogen fueling stations (HFSs) over the transportation network is the foundation for the successful materialization and rapid development of HVs [2],[3]. Catalytic hydrogen (H_2) production from natural gas by methanol steam reforming (MSR) is regarded as an effective H_2 source option for HFSs [4],[5]. However, such technology still relies on fossil fuels and results in excessive emissions of greenhouse gases. The power-to-gas (P2G) technology can split water into H_2 and oxygen (O_2) using the electricity from renewable energy sources (RESs), which is commonly used in HFSs for on-site green H_2 production to supply HVs [6],[7]. In particular, alkaline electrolysis (AEL) represents the most mature P2G technology and has been applied for MW-scale H_2 production [8]. Compared to AEL, polymer electrolyte membrane electrolysis (PEMEL) features shorter start-up time and higher current-densities, producing H_2 with higher purity. Solid oxide electrolysis usually operates at temperatures of 700-900 ℃, leading to higher H_2 production efficiency than AEL/PEMEL but requiring additional heat input [8]. In general, the H_2 and O_2 evolution reactions (HER and OER) of water electrolysis are strictly coupled, and the sluggish four-electron transfer nature of the OER requires a much higher overpotential input than that of the HER to afford the same electrolysis current [9],[10]. Hence, per kg H_2 yield requires the electricity consumption over 45 kWh in most cases, resulting in low electricity-to-H_2 conversion efficiency and bringing a remarkable challenge for the further development and application of P2G on green H_2 production.

Biomass is a sustainable source for H_2 production, and biomass electrolysis has been spotlighted as an emerging technology for producing ultra-pure H_2 under mild conditions [10]-[12]. This electrochemical H_2 production technology substitutes the thermodynamically favorable biomass oxidation reaction for the OER of water electrolysis at the anode, which can significantly reduce the oxidation overpotential with less electricity consumptions compared to P2G [11]. With the ever-increasing installed capacity of RESs in energy systems, more and more renewable generations have to be curtailed to maintain a certain level of system operation reliability [1]. In this context, HFSs can utilize available RES generations, which may otherwise be curtailed, to power biomass electrolysis for H_2 production so as to decrease the electricity purchasing cost and fully exploit the potentially underutilized RESs. Nevertheless, due to the volatile nature of RESs, the dramatic fluctuations in electrolysis current may cause the mechanical wear and chemical degradation of polymer electrolyte membrane (PEM), electrolyte disintegration or even electrode delamination, and thus considerably shorten the lifetimes of electrolyzers [13],[14]. The impact of electrolysis current fluctuations on the service life degradation of H_2 production equipment is another challenge to the green H_2 production from renewables. Consequently, this paper aims to investigate a cost-effective renewable-to-H_2 pathway for HFSs to enhance the electrolysis efficiency and reduce the electrolyzer degradation cost caused by electrolysis current fluctuations, while improving the utilization of local RESs.

B. Relevant background

HFSs are generally deployed over a wide area and operated by private companies to serve the transportation sector [15]. How to produce and supply H_2 to HFSs in an efficient way is the primary concern for the investors. At present, H_2 can either be generated centrally in large industrial plants and then delivered to HFSs by tanker trucks and H_2 pipelines, or directly produced locally in

This work was jointly supported by the Research Grants Council of the HKSAR Government (Grant No. R5020-18), the Innovation and Technology Commission of the HKSAR Government to the Hong Kong Branch of National Rail Transit Electrification and Automation Engineering Technology Research Center (Grant No. K-BBY1), and the National Natural Science Foundation of China (51877072). *(Corresponding author: Bin Zhou.)*

K. Zhang and B. Zhou are with the College of Electrical and Information Engineering, Hunan University, Changsha 410082, China (e-mail: zhankuan1994@qq.com; binzhou@hnu.edu.cn).

S. W. Or is with the Department of Electrical Engineering, The Hong Kong Polytechnic University, Hong Kong, and also with the Hong Kong Branch of National Rail Transit Electrification and Automation Engineering Technology Research Center, Hong Kong (e-mail: eeswor@polyu.edu.hk).

C. Li is with the School of Electronic Information and Electrical Engineering, Shanghai Jiao Tong University, Shanghai 200240, China (e-mail: licanbing@sjtu.edu.cn).

C. Y. Chung is with the Department of Electrical and Computer Engineering, University of Saskatchewan, Saskatoon, Saskatchewan S7N5A9, Canada (e-mail: c.y.chung@usask.ca).

N. Voropai is with the Melentiev Energy Systems Institute of Siberian Branch of the Russian Academy of Sciences, Irkutsk 664033, Russia (e-mail: voropai@isem.irk.ru).

small scale at HFSs [2],[16]. Though the large-scale central production of H_2 is more economical, the expensive transportation cost or huge initial infrastructure investment for dedicated pipelines is more likely to offset the economic advantage [5]. In this context, the distributed on-site H_2 generation is a reasonable option for HFSs as it saves high transportation and pipeline investment costs as well as enhances the reliability of H_2 availability [7],[16].

Generally, H_2 can be produced through the thermochemical, biochemical, or electrolytic conversion processes [17]. Among the existing H_2 production methods, both of MSR and P2G are most commonly used technologies for on-site H_2 production at HFSs. Specifically, the MSR uses natural gas as feedstock to react with high-temperature steam in the presence of the catalyst for H_2 production. This process also contains the water-gas shift reaction where the byproduct CO reacts with the steam to form CO_2, tending to increase greenhouse gas emissions [5]. The P2G technology is of substantial interest to renewable-dominated HFSs. These HFSs can integrate one or several types of renewables for H_2 production, such as H_2-PVT [18], wind-H_2-battery [19], wind-photovoltaic-H_2-battery [20], solar-H_2-fuel cell [21], biomass-H_2-PVT [22], and were investigated with respect to cooperative operation and control, optimal sizing and planning, techno-economic assessment, exergy efficiency promotion, and energy cogeneration. However, the low H_2 production efficiency as well as the impact of dramatic electrolysis current fluctuations on the life degradation cost of electrolyzers is not well addressed.

Also, H_2 production from biomass by thermochemical conversion, such as pyrolysis and gasification, is an effective way to obtain H_2 fuel [23]. The external heat source is indispensable to provide a high-temperature operating condition (i.e., 600-1,000 ℃) for thermochemical conversion of biomass, and thus leads to extra energy consumption costs. Additionally, biomass aqueous electrolysis is acknowledged as an emerging technology for green H_2 production from biomass at intermediate temperatures with no need for the stringent operating condition [11],[24]. Extensive researches on biomass electrolysis in terms of temperature-dependent kinetic modelling, electrochemical reaction mechanism discovery, as well as combining experiment and theory analysis for various native biomass feedstock and electrocatalysts have been reported in [24]-[26] to facilitate H_2 yield rate. Further studies on techno-economic analysis of a solar-powered biomass electrolysis pathway and a streamlined biomass-H_2-electricity conversion design were investigated in [27],[28]. Nevertheless, the synergies and complementarities among biomass and other RESs for on-site H_2 production to meet demands of HVs at HFSs are not involved yet.

C. Contribution

In this paper, an on-site H_2 production method from hybrid RESs along with a hierarchical coordinated control strategy is designed for renewable-dominated HFSs to enhance the green H_2 yield rate and suppress the electrolysis current fluctuation. The key contributions of this study are threefold:

1) A multi-renewable-to-hydrogen production method based on electrochemical effects is proposed to facilitate the H_2 production rate while reducing electricity consumption costs. The available wind and solar outputs are utilized to heat and power biomass electrolysis for H_2 production, significantly enhancing the electrolysis efficiency during the oxidative depolymerization of native biomass and electron (e^-) extraction processes.

2) A capsule network (CN)-based H_2 demand forecasting model is formulated to estimate the gas load for HFS with the spatio-temporal traffic sequence data. The underlying spatial features and temporal dependencies of traffic flows in the transportation network are extracted by multi-dimensional capsule vectors and learned by dynamic routing-by-agreement mechanism iteratively.

3) A two-layer multi-variable coordinated control strategy is developed to suppress high fluctuations in electrolysis current caused by RES uncertainties. Multi-energy conversions and storages for H_2 production are optimized in the upper layer to maximize the operation revenue, while the electrolysis current fluctuation is suppressed with fast-response battery energy storage (BES) in the lower layer based on the MPC framework.

II. Multi-Renewable-to-Hydrogen Modeling

A. Electrochemical hydrogen production mechanism

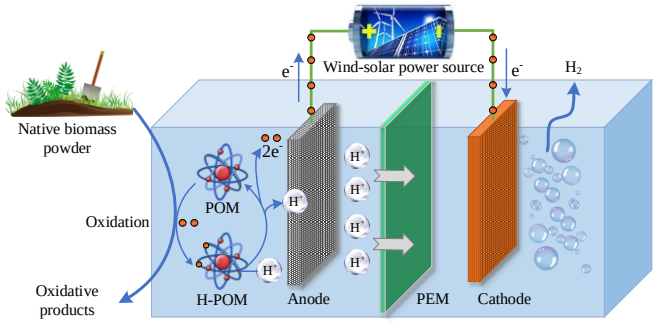

Fig. 1 Schematic illustration of multi-renewable-to-hydrogen production

As shown in Fig. 1, the chemical-electrolysis reaction of multi-renewable-to-hydrogen production is generally conducted in an electrolyzer cell, where a PEM is sandwiched between a graphite-felt anode and a carbon cathode [12]. The biomass electrolysis for green H_2 production can be powered by a DC electric potential provided by wind and solar generations. The conversion pathway and electrochemical reaction rate of polymeric biomass molecules strongly depend on the type of catalysts and electrolysis temperature [11],[26]. Here, the aqueous polyoxometalate (POM), one of the best-performing and inexpensive water-soluble molecular metal-oxide clusters, is adopted as the catalyst and e^- mediator for accelerating the oxidative depolymerization of biomass and e^- extraction [24]. In the aqueous POM electrolyte solution, the native biomass, including lignocellulose, grass and wood powders, can be directly oxidized for electrolytic H_2 production and exhibit the improved thermodynamics at elevated electrolysis temperatures. More specifically, the conversion process at the anode side begins with the biomass oxidation by POM to form a reduced POM complex (H-POM), while water molecule also serves as a proton (H^+) donor in this process according to the reaction: Biomass+H_2O+POM→Oxidized products+CO_2+H-POM. Note that the byproduct CO_2 can be captured and absorbed by low-cost hydroxide adsorbents or ionic liquids, and applied to the energy industry such as methane production and enhanced oil recovery [22],[29]. Then, the reduced H-POM can be readily reoxidized at anode surface driven by the applied electric field. Meanwhile e^- and H^+ are released from H-POM into the anode electrode and electrolyte solution respectively on the basis of the reaction: H-POM→POM+H^++e^-. Finally, the released H^+ mitigate through the PEM to the cathode side and combine with e^- from the external circuit to form H_2 based on the reaction: $2H^+$+$2e^-$→H_2.

B. Modeling of multi-renewable-to-hydrogen production

The electrolyzer cell voltage $u_{c,t}$ is sensitive and nonlinear to the operation temperature $T_{c,t}$ and electrolysis current $I_{elz,t}$, and corresponds to the sum of the reversible voltage $u_{rev,t}$ and irreversible voltage $u_{irrev,t}$ [30]. The reversible voltage, namely the open circuit voltage, denotes the ideal minimum energy needed by the electrolytic reaction of biomass thermodynamically. The irreversible voltage represents the extra energy required to overcome the kinetic reaction barriers and make the electrolysis reaction actually occur. Here, $u_{rev,t}$ can be obtained in an open circuit thermodynamic balance and calculated by a modified Nernst equation [18]. $u_{irrev,t}$ is modeled with an empirical formula using polynomial and logarithm combinations by fitting the experimental data in [24],[30]. In general, an electrolyzer stack shall be built consisting of the number of N_c series cells to ensure sufficient H_2 production, and the temperature-dependent electrode kinetics of the stack can be modeled, as follows,

$$u_{c,t} = u_{rev,t} + u_{irrev,t} \tag{1}$$

$$u_{rev,t} = \frac{\Delta G_{bio}}{zF} + \frac{\Delta S_{bio}}{zF}(T_{c,t} - T_{ref}) + \frac{RT_{c,t}}{zF}\ln[(H_{elz}/H_{ref})] \tag{2}$$

$$u_{irrev,t} = \frac{a_1 + a_2 T_{c,t}}{A_c} I_{c,t} + \sigma \log\left(\frac{b_1 + b_2/T_{c,t} + b_3/T_{c,t}^2}{A_c} I_{c,t} + 1\right) \tag{3}$$

$$u_{s,t} = N_c u_{c,t} \tag{4}$$

$$P_{elz,t} = u_{s,t} I_{c,t} \tag{5}$$

where ΔG_{bio} and ΔS_{bio} represent the changes in free Gibbs energy and entropy of the biomass electrolysis reaction, respectively; z is the number of transferred e^- per mole of H_2 generated; R and F denote the ideal gas constant and Faraday constant, respectively; T_{ref} and H_{ref} are the standard reference temperature and pressure; H_{elz} and A_c represent the partial pressure of the produced H_2 and area of electrode; a_1 and a_2 are parameters associated with the ohmic resistance; b_1, b_2, b_3, and σ are parameters related to activation and concentration overvoltage; $u_{s,t}$ and $P_{elz,t}$ represent the electrolytic stack voltage and power.

On the basis of Faraday's law, the H_2 production rate of an electrolyzer cell is approximately proportional to the electrolysis current, and thus the hydrogen production rate $m_{s,t}$ at time t in a stack can be expressed as follows,

$$m_{s,t} = (N_c \eta_{F,t} I_{c,t} M_{H_2})/zF \tag{6}$$

$$\eta_{F,t} = \frac{(I_{c,t}/A_c)^2}{(a_3 + a_4 T_{c,t}) + (I_{c,t}/A_c)^2}(b_4 + b_5 T_{c,t}) \tag{7}$$

$$\eta_{elz,t} = m_{s,t} Q_{H_2} / P_{elz,t} \tag{8}$$

where M_{H_2} denotes the molar mass of H_2; $\eta_{F,t}$ is the Faraday efficiency at time t, which is defined as the ratio of the actual amount of H_2 produced to the theoretical value. An empirical expression of $\eta_{F,t}$ is derived by fitting the measured data of the experiments in [24],[30], where a_3, a_4, b_4, and b_5 are empirical parameters. $\eta_{elz,t}$ and Q_{H_2} represent the electrolysis efficiency and heating value of H_2, respectively.

Apart from providing electric power for biomass electrolysis, the available wind and solar generations can also be harvested for heating the electrolyzer to enhance the H_2 production rate and efficiency. A resistance-capacitance (R-C) thermodynamic network model is developed to investigate the thermal interactions within the electrolyzer under the internal Joule heat generations and external RES energy injections, as illustrated in Fig. 2. Since the structure/material and surroundings of the electrolyzer at all directions can be regarded as the same, the heat storage and transfer of electrolyte and peripheral wall are handled with the classical lumped parameter method in [31] by using equivalent thermal capacitances C_c, C_w and resistances Z_c, Z_w, Z_o at one direction. The temperatures of electrolyte, wall, and ambient air $T_{c,t}$, $T_{w,t}$, $T_{o,t}$ are denoted by nodes at their geometrical center. The peripheral wall node links to the internal and external nodes via thermal resistances $(Z_c + Z_w/2)$ and $(Z_o + Z_w/2)$ to denote inside and outside conductive/convective heat transfer properties. Then, the thermal interactions among the electrolyte, wall, and ambient air can be governed by nodal analysis, as follows,

$$C_c \frac{dT_{c,t}}{dt} = \frac{T_{w,t} - T_{c,t}}{Z_c + Z_w/2} + \frac{E_{RES,t}\Delta t}{N_c} + I_{c,t} u_{c,t} \Delta t - \frac{m_{s,t} Q_{H_2} \Delta t}{N_c} \tag{9}$$

$$E_{RES,t} = (E_{hf,t} + E_{ef,t}\eta_B) \tag{10}$$

$$C_w \frac{dT_{w,t}}{dt} = \frac{T_{c,t} - T_{w,t}}{Z_c + Z_w/2} + \frac{T_{o,t} - T_{w,t}}{Z_o + Z_w/2} \tag{11}$$

where $E_{RES,t}$ represents the controllable RES energy feedbacks, including electricity $E_{ef,t}$ and heating energy $E_{hf,t}$, for heating electrolyzers at the tth time slot; Δt is the length of per time slot; η_B is the conversion efficiency of the electric boiler. The four terms on the right hand of (9) denote the heat flux from the wall to the electrolyte driven by temperature differences, heating energy injections from RES feedbacks, Joule heating caused by electrolysis current, and enthalpy change for endothermic H_2 evolution reaction. Hence, with the thermodynamic model in (9)-(11), the operation temperature dynamics of electrolysis climate can be captured and predicted, offering an essential basis to coordinately control the electrolysis temperature and current for H_2 production enhancement.

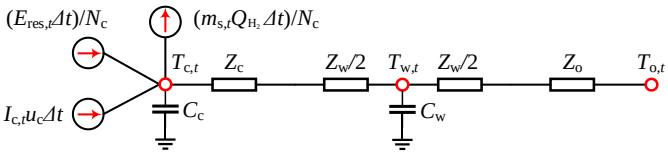

Fig. 2 R-C thermodynamic network model of the electrolyzer

All in all, a multi-renewable-to-hydrogen production model based on electrochemical effects is formulated in (1)-(11) to analyze the H_2 yield rate and electrolysis efficiency under different operation temperatures, currents, and voltages. In this model, the available wind and solar outputs can be harvested to heat and power biomass electrolysis for H_2 production so as to enhance the electrolysis efficiency during the oxidative depolymerization of native biomass and e^- extraction processes while facilitating the utilization of local RESs. The temperature dynamics within the electrolysis climate can be captured using the developed R-C thermodynamic network.

III. Hierarchical Coordinated Control Strategy

A. Multi-renewable-to-hydrogen production system

Fig. 3 depicts the developed multi-renewable-to-hydrogen production system for on-site HFS to satisfy H_2 fuel demands from HVs. Wind and solar energy can be harvested by the wind turbine (WT) and photovoltaic thermal (PVT) unit to power the biomass electrolysis for H_2 production in the electrolyzer stack.

$$\begin{bmatrix} L_{\mathrm{g},t} \\ L_{\mathrm{e},t} \\ E_{\mathrm{RES},t} \end{bmatrix} = \underbrace{\begin{bmatrix} 0 & 0 & 0 & v_{\mathrm{g},t} & 0 & 0 & v_{\mathrm{g},t} \\ v_{\mathrm{e},t} & 0 & v_{\mathrm{e},t} & v_{\mathrm{FC},t}Q_{\mathrm{H_2}}\eta^{\mathrm{e}}_{\mathrm{FC}}v_{\mathrm{e},t} & v_{\mathrm{e},t} & v_{\mathrm{e},t} & v_{\mathrm{FC},t}Q_{\mathrm{H_2}}\eta^{\mathrm{e}}_{\mathrm{FC}}v_{\mathrm{e},t} \\ v_{\mathrm{B},t} & 1 & v_{\mathrm{B},t} & Q_{\mathrm{H_2}}v_{\mathrm{FC},t}(\eta^{\mathrm{h}}_{\mathrm{FC}}+\eta^{\mathrm{e}}_{\mathrm{FC}}v_{\mathrm{B},t}\eta_{\mathrm{B}}) & v_{\mathrm{B},t} & v_{\mathrm{B},t} & Q_{\mathrm{H_2}}v_{\mathrm{FC},t}(\eta^{\mathrm{h}}_{\mathrm{FC}}+\eta^{\mathrm{e}}_{\mathrm{FC}}v_{\mathrm{B},t}\eta_{\mathrm{B}}) \end{bmatrix}}_{\mathbf{M}} \begin{bmatrix} P^{\mathrm{e}}_{\mathrm{PVT},t} \\ P^{\mathrm{h}}_{\mathrm{PVT},t} \\ P_{\mathrm{WT},t} \\ m_{\mathrm{s},t} \\ P_{\mathrm{gd},t} \\ P_{\mathrm{BES},t} \\ m_{\mathrm{HST},t} \end{bmatrix} \tag{12}$$

Here, the PVT unit is referred as a renewable cogeneration unit combining photovoltaic (PV) modules and thermal collectors to concurrently produce electricity and low-temperature heat from solar radiation energy [9]. Water acts as a medium to extract heat from PVT unit, and the mass flow rate of water replenishment can be controlled to obtain the required quantities and qualities of thermal energy. Moreover, the thermal energy generated by the PVT unit and waste heat recovered from the fuel cell (FC) are transmitted in the form of hot water through annular water pipelines to heat the electrolyzer stack so as to accelerate the electrochemical reaction rate of H_2 production. The water circulation can be driven by water pumps and its flow rate is governed by valve regulation [22]. The produced gaseous H_2 can be reserved in the hydrogen storage tank (HST) for later use to meet high H_2 fuel demands from the transportation network, or converted back into electricity by FC to opportunistically perform energy arbitrage in the electricity market. The compressor is installed at the upstream of dedicated H_2 pipelines to provide the pressure needed to transport/store H_2 fuel and control the mass flow rate by adjusting the pipe pressure [6]. Besides, to decrease the degradation cost of electrolyzer stack, the fast-response BES is utilized to mitigate dynamic fluctuations in electrolysis current induced by the intermittent and volatile nature of RESs. Consequently, multi-energy couplings and feedback connections are established to promote the operating controllability and flexibility of the HFS for efficient H_2 production from hybrid renewables.

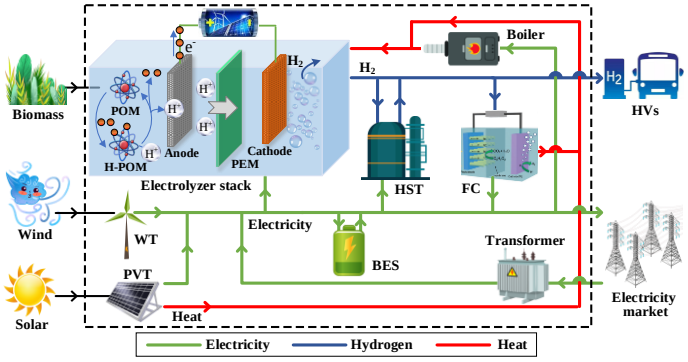

Fig. 3 Multi-renewable-to-hydrogen production system for HFS

A multi-energy coupling matrix **M** is formulated to indicate energy conversion efficiencies, energy allocations, and system-internal topology, as shown in (12). Specifically, $\eta^{\mathrm{e}}_{\mathrm{FC}}$ and $\eta^{\mathrm{h}}_{\mathrm{FC}}$ denote the gas-electric and gas-heating conversion efficiencies of the FC; $v_{\mathrm{FC},t}$, $v_{\mathrm{B},t}$, $v_{\mathrm{g},t}$, and $v_{\mathrm{e},t}$ represent the energy allocation coefficients of input energy for FC, electric boiler, HVs, and electricity market at time t; The input energy includes electrical and thermal outputs of WT and PVT $P_{\mathrm{WT},t}$, $P^{\mathrm{e}}_{\mathrm{PVT},t}$, $P^{\mathrm{h}}_{\mathrm{PVT},t}$, net outputs of BES and HST $P_{\mathrm{BES},t}$ and $m_{\mathrm{HST},t}$, H_2 output of the electrolyzer stack, as well as the electricity purchased from local grid $P_{\mathrm{gd},t}$ for H_2 production in case of insufficient RES generations under extreme weather conditions; $L_{\mathrm{g},t}$ and $L_{\mathrm{e},t}$ are the H_2 demands and electricity sold of HFS at time t.

As the product of energy allocation coefficients increases the nonlinearity of the multi-energy coupling model (12), a state variable-based approach is exploited to avert this nonlinearity by designating state variables for inputs/outputs of multi-energy conversion devices [31]. Taking the FC as an instance, its electricity output at time t can be denoted as a state variable $E_{\mathrm{FC},t}$, and the input energy from H_2 fuel can be represented by $E_{\mathrm{FC},t}/\eta^{\mathrm{e}}_{\mathrm{FC}}$ without introducing the energy allocation coefficient $v_{\mathrm{FC},t}$. In this way, the input power consumptions of the compressor and electrolyzer stack $P_{\mathrm{com},t}$ and $P_{\mathrm{elz},t}$, electrical and heating energy feedbacks for electrolyzer heating $E_{\mathrm{ef},t}$ and $E_{\mathrm{hf},t}$, are combined with the input variables in (12) to form a new state variable vector, as shown in (13). Moreover, a new multi-energy coupling matrix **M'** is formed to depict the couplings and synergies among these state variables, which is sparser for efficient computations and exhibits greater scalability with integration of additional energy converters compared to matrix **M**.

$$\begin{bmatrix} L_{\mathrm{g},t} \\ L_{\mathrm{e},t} \\ E_{\mathrm{RES},t} \\ 0 \end{bmatrix} = \underbrace{\begin{bmatrix} 0 & 0 & 0 & 1 & 0 & 0 & 1 & 0 & 0 & \dfrac{-1}{\eta^{\mathrm{e}}_{\mathrm{FC}}Q_{\mathrm{H_2}}} & 0 & 0 \\ 1 & 0 & 1 & 0 & 1 & 1 & 0 & -1 & -1 & 1 & -1 & 0 \\ 0 & 0 & 0 & 0 & 0 & 0 & 0 & 0 & 0 & 0 & \eta_{\mathrm{B}} & 1 \\ 0 & 1 & 0 & 0 & 0 & 0 & 0 & 0 & 0 & \dfrac{\eta^{\mathrm{h}}_{\mathrm{FC}}}{\eta^{\mathrm{e}}_{\mathrm{FC}}} & 0 & -1 \end{bmatrix}}_{\mathbf{M'}} \begin{bmatrix} P^{\mathrm{e}}_{\mathrm{PVT},t} \\ P^{\mathrm{h}}_{\mathrm{PVT},t} \\ P_{\mathrm{WT},t} \\ m_{\mathrm{s},t} \\ P_{\mathrm{gd},t} \\ P_{\mathrm{BES},t} \\ m_{\mathrm{HST},t} \\ P_{\mathrm{elz},t} \\ P_{\mathrm{com},t} \\ E_{\mathrm{FC},t} \\ E_{\mathrm{ef},t} \\ E_{\mathrm{hf},t} \end{bmatrix} \tag{13}$$

B. *Hydrogen demand forecasting model*

The construction of HFSs is usually located at road junctions to capture traffic flows as many as possible for maximizing the economic revenue, and the short-term prediction of H_2 demands from HVs is essential for HFSs to make optimal decisions on H_2 production and storage. Though the refueling events in HFSs are hardly to be foreseen directly due to the random driving and parking behaviors of HVs, the H_2 load of an HFS is strongly influenced by the traffic state of its neighboring roadways [5],[32]. Therefore, a CN-based H_2 demand forecasting model based on the spatio-temporal traffic sequence data is presented to estimate the time-varying gas loads of HFS. Firstly, the traffic flow of a roadway link is defined as the number of vehicles passing through that link, and the transportation network is segmented by lots of grids with a specific spatial latitude and longitude range, e.g., $0.0001° \times 0.0001°$ [33]. The value of each grid represents the number of vehicles on the roadway passing through this grid, and thus these grids can be served as pixels to

indicate the traffic state. In this way, the transportation network at a given time point is displayed as an image, and image sequences over a historical time period can be used as data samples for CN training and testing.

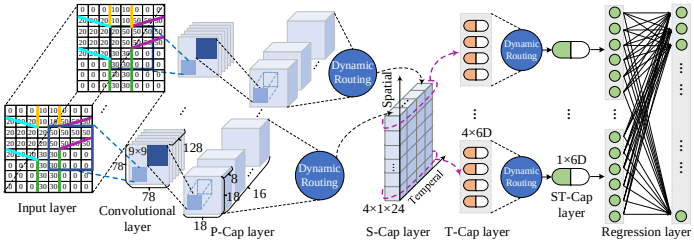

Fig. 4 CN-based H_2 demand forecasting architecture

Then, a CN architecture, composing of the convolutional layer, capsule layers, and fully connected layer, is designed to extract the spatial features of traffic flows and capture the temporal dependencies in traffic sequence data for H_2 demand prediction, as shown in Fig. 4. Here, different abstract features induced by spatial influence factors, such as connection topology, spatial structure, traffic capacity, distance and length of roadway links, are implied in traffic flows, which are known as the spatial features of the traffic flows [34]. Due to the interactive effects among traffic flows in different roadway links, in especial the adjacent or connected links, the first convolutional layer is used to preliminarily extract the low-level local spatial features of traffic flows over small regions from the input traffic images. The convolutional operations with sliding windows are then performed in the primary capsule (P-Cap) layer to convert the scalar outputs of neurons into primary capsules in the vector form. Here, a capsule is a multi-dimensional vector neuron encapsulating the instantiation parameter information to represent the distinguishing features of an object [33]. The length of a capsule indicates the detection probability of a feature, while its direction encodes the state of the feature, such as road rotation angle, length, and topology. The spatial capsule (S-Cap) layer is used to capture the spatial relationships among local spatial features implied in P-Caps and form a set of advanced capsules by dynamic routing-by-agreement mechanism, as follows,

$$\hat{\boldsymbol{\mu}}_{j|i} = \mathbf{W}_{ij}\boldsymbol{\mu}_i \tag{14}$$

$$\varphi_{ij}^r = \frac{\exp(\varepsilon_{ij}^r)}{\sum_j \exp(\varepsilon_{ij}^r)} \tag{15}$$

$$\boldsymbol{\psi}_j^r = \sum_i \varphi_{ij}^r \hat{\boldsymbol{\mu}}_{j|i} \tag{16}$$

$$\mathbf{v}_j^r = \frac{\left\|\boldsymbol{\psi}_j^r\right\|^2}{1+\left\|\boldsymbol{\psi}_j^r\right\|^2} \frac{\boldsymbol{\psi}_j^r}{\left\|\boldsymbol{\psi}_j^r\right\|} \tag{17}$$

$$\varepsilon_{ij}^r = \varepsilon_{ij}^r + \mathbf{v}_j^r \cdot \hat{\boldsymbol{\mu}}_{j|i} \tag{18}$$

where $\boldsymbol{\mu}_i$, $\hat{\boldsymbol{\mu}}_{j|i}$, and $\mathbf{W}_{ij}$ represent the local spatial feature extracted by a P-Cap i, predicted feature for an advanced capsule j by P-Cap i, and weight matrix of the affine transformation, respectively. In the rth iteration, routing logit ε_{ij}^r and coupling coefficient φ_{ij}^r denote the log prior probability and normalized probability of capsule i coupled to capsule j; Determined by the softmax function (17), the coupling coefficients between capsule i and all the advanced capsules in S-Cap layer sum to 1; The input vector $\boldsymbol{\psi}_j^r$ to an advanced capsule j is the weighted sum over all predicted vectors $\hat{\boldsymbol{\mu}}_{j|i}$ from P-Caps layer; $\mathbf{v}_j^r$ is the output vector of capsule j after the nonlinear squashing operation to ensure that the length of the vector can denote the existence probability of the extracted features. Note that the dot product $\mathbf{v}_j^r \cdot \hat{\boldsymbol{\mu}}_{j|i}$ is treated as the agreement between the current output $\mathbf{v}_j^r$ of advanced capsule j and the prediction $\hat{\boldsymbol{\mu}}_{j|i}$ from P-Cap i. Hence, the routing logits and coupling coefficients can be iteratively refined by measuring this agreement and a set of spatial capsules are generated to exhibit the global spatial features of traffic flows.

Subsequently, the extracted spatial features at different time points are chronologically encoded in time dimension with time capsules (T-Caps) to capture potential nonlinear temporal characteristics of traffic flows. Similarly, through the iterative dynamic routing process, the spatio-temporal capsules (ST-Caps) can be formed, containing the spatio-temporal correlations of traffic flows. A linear layer reshapes the multi-dimensional spatio-temporal data to one-dimensional form for the convenience of a full-connected regression layer to derive the final predicted value of traffic flows in multiple roadway links. Finally, the H_2 load of an HFS at time t can be forecasted on the basis of the mean arrival rate $\kappa_{l,t}$ and traffic flow $f_{l,t}$ on each roadway link, as follows,

$$L_{g,t} = m_{\mathrm{HV},t}(\omega_{\mathrm{HV}} \sum\nolimits_l \kappa_{l,t}(f_{l,t}, Ta_{l,t})) \tag{19}$$

$$\rho_{l,t} = \frac{f_{l,t}}{Le_l} \tag{20}$$

$$\rho_{l,\max} = \frac{\chi_l}{Le_l} \tag{21}$$

$$v_{l,t} = \begin{cases} v_{l,\mathrm{free}}\left(1-\dfrac{\rho_{l,t}}{\rho_{l,\max}}\right), & 0 < \rho_{l,t} \le \rho_{l,\mathrm{jam}} \\ -v_{l,\mathrm{free}}\left(\dfrac{\rho_{l,\mathrm{jam}}}{\rho_{l,\max}}\right)\left(1-\dfrac{\rho_{l,\max}}{\rho_{l,t}}\right), & \text{otherwise} \end{cases} \tag{22}$$

$$Ta_{l,t} = \frac{Le_l}{v_{l,t}} \tag{23}$$

where $\rho_{l,t}$ and $v_{l,t}$ denote the traffic flow density and mean velocity on roadway link l at time t, respectively; $v_{l,\mathrm{free}}$, $\rho_{l,\max}$, and $\rho_{l,\mathrm{jam}}$ are the maximum free-flow velocity, maximum density, and critical density at which the traffic flow transitions from free-flow state to congested state; χ_l and Le_l represent the traffic capacity and length of roadway link l; $m_{\mathrm{HV},t}$ is the H_2 dispersing rate for an HV in HFS at time t; ω_{HV} denotes the proportion of HVs among all vehicles in the local region at which the HFS locates. Generally, ω_{HV} and $\rho_{l,\mathrm{jam}}$ are empirical values based on the observed historical traffic data [35]. A modified Daganzo-Newell velocity model with a linear function in free-flow state and a hyperbolic expression in congestion state is adopted to calculate $v_{l,t}$, as shown in (22) [34],[36]. $Ta_{l,t}$ is the mean arrival time of vehicles on roadway link l, and the expected number of arrival vehicles in each time slot, i.e., the mean arrival rate, can be estimated based on the obtained $Ta_{l,t}$.

C. *Optimization objective*

A two-layer multi-variable coordinated control strategy incorporating the electrolysis current, voltage, temperature, and multi-energy outputs of various conversion and storage devices is developed for the economic operation of the renewable-dominated HFS. Fig. 5 schematically depicts the hierarchical structure of the developed control strategy based on the MPC

framework, in which Δt_{lo} and Δt_{up} represent the length of each control time slot in the lower and upper layers, respectively. In the upper layer, the optimal discrete-time operation trajectories of the electrolyzer stack, HST, BES, FC, and electric boiler over the time horizon t_{up} can be obtained, and the upper optimization is recursively carried out every Δt_{up} with rolling procedures. It is worth noting that only the control instructions for the first time slot of t_{up} will be forwarded and performed as the reference values in the lower layer [37]. Then, the time horizon rolls forward to the next slot, and the current time slot Δt_{up} is equally divided into n smaller time slots Δt_{lo} in the lower layer. Afterward, the lower layer makes its own optimization to closely match the reference operation trajectories and actual ones after the realization of RES and H_2 load forecast errors in each Δt_{lo}. After time Δt_{up}, the lower layer feeds back the resulting state variables such as SOC of H_2 and electricity storages back to the upper layer for HFS control optimization in the next iteration.

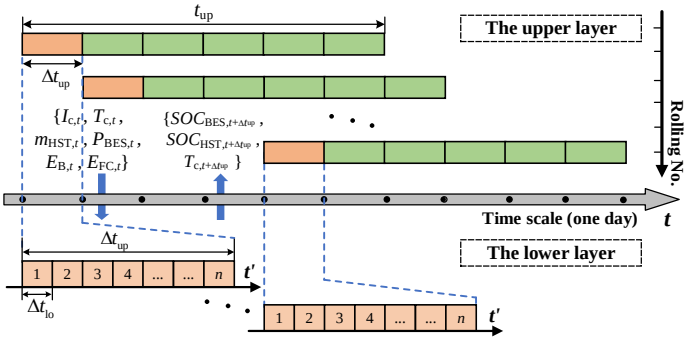

Fig. 5 Hierarchical structure of the proposed coordinated control strategy

More specifically, based on the forecasting of the forthcoming RES generations and H_2 fuel demands over t_{up}, the aim of the upper layer is to maximize the total profit of the HFS, including the expected revenue from selling H_2 fuel to HVs and making energy arbitrage in the electricity market. The associated system operation cost contains the degradation costs of the BES and electrolyzer stack, BDC_t and SDC_t, as shown in (25) and (26),

$$\mathrm{Max} \sum_{t\in t_{\mathrm{up}}} \left\{ \lambda_t^{\mathrm{g}} L_{\mathrm{g},t} \Delta t_{\mathrm{up}} + \lambda_t^{\mathrm{e}} (L_{\mathrm{e},t} - P_{\mathrm{gd},t}) \Delta t_{\mathrm{up}} - BDC_t - SDC_t \right\} \quad (24)$$

$$BDC_t = \frac{r_{\mathrm{b}}[Co_{\mathrm{b}} E_{\mathrm{b}} (1+r_{\mathrm{b}})^{\frac{(1-\eta_{\mathrm{b}})E_{\mathrm{b}}}{\omega E_{\mathrm{b}}^{\mathrm{av}}}} - Co_{\mathrm{b}} S_{\mathrm{b}}]}{E_{\mathrm{b}}^{\mathrm{av}}[(1+r_{\mathrm{b}})^{\frac{(1-\eta_{\mathrm{b}})E_{\mathrm{b}}}{\omega E_{\mathrm{b}}^{\mathrm{av}}}} - 1]} (\eta_{\mathrm{ch}} P_{\mathrm{ch},t} + \frac{P_{\mathrm{dis},t}}{\eta_{\mathrm{dis}}}) \Delta t_{\mathrm{up}} \quad (25)$$

$$\begin{aligned} SDC_t = {} & \tau_{\mathrm{s},t} N_{\mathrm{c}} Co_{\mathrm{c}} / \vartheta_{\mathrm{c}} \, \Delta t_{\mathrm{up}} + N_{\mathrm{c}} d_{\mathrm{su}} \tau_{\mathrm{s},t} (1 - \tau_{\mathrm{s},t-1}) + \\ & N_{\mathrm{c}} d_{\mathrm{sd}} \tau_{\mathrm{s},t-1} (1 - \tau_{\mathrm{s},t}) + N_{\mathrm{c}} d_{\mathrm{f}} [\mathrm{sgn}(I_{\mathrm{c},t} - I_{\mathrm{c}}^{\mathrm{ra}})](I_{\mathrm{c},t} - I_{\mathrm{c}}^{\mathrm{ra}}) \end{aligned} \quad (26)$$

where λ_t^{g} and λ_t^{e} are the market prices of H_2 and electricity at time t. Here, the degradation cost caused by charging/discharging actions of BES is modelled as a series of equal payments during its lifetime based on the engineering economic principle [38]. Co_{b} and Co_{c} denote the capital costs for BES and electrolyzer cell; E_{b}, $E_{\mathrm{b}}^{\mathrm{av}}$, S_{b}, r_{b}, and ω represent the rated capacity, average amount of daily processed energy, salvation value ratio, equivalent daily discount rate, and wear coefficient of BES, respectively; $P_{\mathrm{ch},t}$, $P_{\mathrm{dis},t}$, η_{ch}, and η_{dis} indicate the charging/discharging power and efficiencies of BES, respectively. Compared to the BES, the electrolyzer has different degradation mechanism and its degradation cost is primarily resulted from the operation time, start-stop condition, and in especial electrolysis current fluctuation [13]. d_{su}, d_{sd}, and d_{f} are unit costs of electrolyzer startup, shutdown, and electrolysis current fluctuation, respectively [31]; $\tau_{\mathrm{s},t}$ is a binary variable, 0 or 1, to denote the operation state of the stack; $I_{\mathrm{c}}^{\mathrm{ra}}$ and ϑ_{c} represent the rated electrolysis current and estimated lifetime of the electrolyzer cell given by the manufacturer.

The objective of the lower layer is to minimize the deviations from the reference operating setpoints and suppress high fluctuations in electrolysis current after the realization of RES and H_2 load forecast errors in each Δt_{lo}. Due to the short time-scale variability of wind and solar generations, the dispatchable BES with fast response time and high energy density is rescheduled to compensate the electrolytic power shortage and suppress the electrolysis current fluctuation for reliable and efficient H_2 production, as follows,

$$\mathrm{Min} \left\{ \begin{array}{l} BDC_{t'}/(BDC_t/n) + \sigma_{\mathrm{I}} (I_{\mathrm{c},t'} - I_{\mathrm{c},t})^2 / I_{\mathrm{c,max}} \\ + \sigma_{\mathrm{T}} (T_{\mathrm{c},t'} - T_{\mathrm{c},t})^2 / T_{\mathrm{c,max}} + \boldsymbol{\sigma} \cdot [(\boldsymbol{\varsigma}_{t'} - \boldsymbol{\varsigma}_t)^2 / \boldsymbol{\varsigma}_{\max}] \end{array} \right\} \quad (27)$$

where t' denotes the t'th time slot in the lower layer; $\boldsymbol{\varsigma}_t$ and $\boldsymbol{\varsigma}_{t'}$ are the referenced and actual vectors incorporating multi-energy output variables of FC, HST, and boiler at time slot t and t', respectively; σ_{I}, σ_{T}, and $\boldsymbol{\sigma}$ are cost weighting coefficients/vectors; $I_{\mathrm{c,max}}$, $T_{\mathrm{c,max}}$, and $\boldsymbol{\varsigma}_{\max}$ represent the upper bounds of the state variables. Compared with the conventional current-controlled-alone H_2 production method, the electrolysis current and temperature are coordinated controlled to maintain the scheduled H_2 yield rate and electrolysis efficiency. After time $n\Delta t_{\mathrm{lo}}$, the lower layer feeds back the updated state variables, such as the electrolysis temperature, SOC of BES and HST, to the upper layer for H_2 production and storage optimization in the next t_{up}. This rolling and control procedure will be repeated iteratively based on the continuously updated forecasting of RES outputs and H_2 fuel demands at HFSs.

D. System constraints

1) Multi-energy output constraints: The outputs of the FC, electric boiler, BES, and HST should be subject to their output limits $E_{\mathrm{FC,max}}$, $E_{\mathrm{B,max}}$, $P_{\mathrm{ch,max}}$, $P_{\mathrm{dis,max}}$, $m_{\mathrm{HST,min}}$ and $m_{\mathrm{HST,max}}$ [15],[39]. Besides, the electrolysis temperature should not exceed the allowable maximum operation temperature $T_{\mathrm{c,max}}$ to protect the PEM from dehydration which may result in low proton conductivity, as follows,

$$0 \le E_{\mathrm{FC},t} \le E_{\mathrm{FC,max}} \quad (28)$$

$$0 \le \eta_{\mathrm{B}} E_{\mathrm{ef},t} \le E_{\mathrm{B,max}} \quad (29)$$

$$0 \le P_{\mathrm{ch},t} \le P_{\mathrm{ch,max}} \varphi_{\mathrm{ch},t} \quad (30)$$

$$0 \le P_{\mathrm{dis},t} \le P_{\mathrm{dis,max}} \varphi_{\mathrm{dis},t} \quad (31)$$

$$\varphi_{\mathrm{ch},t} + \varphi_{\mathrm{dis},t} \le 1 \quad (32)$$

$$m_{\mathrm{HST,min}} \le m_{\mathrm{HST},t} \le m_{\mathrm{HST,max}} \quad (33)$$

$$0 \le T_{\mathrm{c},t} \le T_{\mathrm{c,max}} \quad (34)$$

where $\varphi_{\mathrm{ch},t}$ and $\varphi_{\mathrm{dis},t}$ are binary variables to denote the charging and discharging states of the BES at time t.

2) H_2 and electricity storage constraints: The state of charge (SOC) of BES and HST in each time slot should be constrained within their physical lower and upper bounds to avoid being over-charged and over-discharged [40]. The H_2 storage pressure $H_{\mathrm{HST},t}$ should also be constrained within the allowable lower and upper bounds, $H_{\mathrm{HST,min}}$ and $H_{\mathrm{HST,max}}$, as follows,

$$SOC_{\mathrm{BES,min}} \le SOC_{\mathrm{BES},t} \le SOC_{\mathrm{BES,max}} \quad (35)$$

$$SOC_{\mathrm{HST,min}} \le SOC_{\mathrm{HST},t} \le SOC_{\mathrm{HST,max}} \tag{36}$$

$$SOC_{\mathrm{BES},t} = SOC_{\mathrm{BES},t-1} + [(\eta_{\mathrm{ch}} P_{\mathrm{ch},t} - P_{\mathrm{dis},t}/\eta_{\mathrm{dis}})\Delta t]/E_{\mathrm{b}} \tag{37}$$

$$SOC_{\mathrm{HST},t} = SOC_{\mathrm{HST},t-1} - m_{\mathrm{HST},t}\Delta t / m_{\mathrm{HST}}^{\mathrm{ra}} \tag{38}$$

$$P_{\mathrm{com},t} = \frac{kRT_{\mathrm{c},t}}{\eta_{\mathrm{cmp}}(k-1)}\left[\left(\frac{H_{\mathrm{HST},t}}{H_{\mathrm{elz}}}\right)^{\frac{k-1}{k}} - 1\right] m_{\mathrm{s},t} \tag{39}$$

$$H_{\mathrm{HST},t} = H_{\mathrm{HST},t\text{-}1} + \frac{RT_{\mathrm{HST}}}{V_{\mathrm{HST}} M_{\mathrm{H_2}}}(SOC_{\mathrm{HST},t-1} m_{\mathrm{HST}}^{\mathrm{ra}} - m_{\mathrm{HST},t}\Delta t) \tag{40}$$

$$H_{\mathrm{HST,min}} \le H_{\mathrm{HST},t} \le H_{\mathrm{HST,max}} \tag{41}$$

where $SOC_{\mathrm{BES},t}$ and $SOC_{\mathrm{BES},t-1}$ are the SOC of BES at time t and t-1, respectively; $SOC_{\mathrm{HST},t}$ and $SOC_{\mathrm{HST},t-1}$ are the SOC of HST at time t and t-1, respectively; $SOC_{\mathrm{BES,min}}$ and $SOC_{\mathrm{BES,max}}$ represent the lower and upper SOC bounds for electricity storage of BES; $SOC_{\mathrm{HST,min}}$ and $SOC_{\mathrm{HST,max}}$ denote the lower and upper SOC bounds for H_2 storage of HST; T_{HST}, V_{HST}, and $m_{\mathrm{HST}}^{\mathrm{ra}}$ denote the standard operation temperature, volume and rated energy capacity of HST, respectively; The input power of the compressor is calculated based on the polytropic compression model in [15]. k and η_{com} are the polytropic coefficient and compression efficiency, respectively.

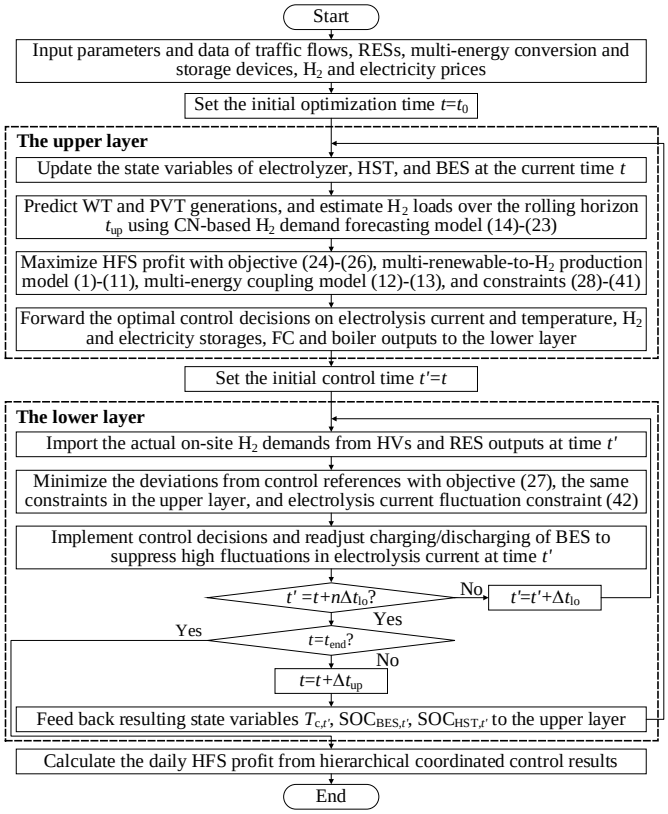

Fig. 6 Flowchart of two-layer coordinated control strategy

The operational constraints (28)-(41) should be observed for both upper and lower layers. In addition, due to the volatile electrolysis power provided by RESs, the sudden increasing or decreasing of the electrolysis current within a short-time period would cause the mechanical wear and chemical degradation of the PEM and electrode [14]. To alleviate the impact of electrolysis current fluctuations on the degradation of the electrolyzer stack, the current change between two consecutive time slots should be controlled within the allowed maximum value $I_{\mathrm{c,lim}}$ in the lower layer, as follows,

$$\left|I_{\mathrm{c},t'} - I_{\mathrm{c},t'-1}\right| \le I_{\mathrm{c,lim}} \tag{42}$$

In summary, the implementation flowchart of the proposed two-layer coordinated control strategy is outlined in Fig. 6. The upper layer maximizes the expected profit of the HFS over a finite time horizon, and passes the optimal operating set points of HFS equipment to the lower layer as control references. The lower layer follows the control instructions from the upper layer while suppressing high electrolysis current fluctuations at smaller timescales. The system state variables are updated after the lower optimization and fed back to the upper layer for the next rolling optimization. In this way, the optimization decisions made by two layers dynamically interact with each other to improve the economic benefit of HFS.

IV. Case Study

A. System data

A small-scale test system with the same configuration as illustrated in Fig. 3 is presented to verify the superior performance of the proposed methodology. In this system, the installed capacities of WT and PVT are 2 MW and 3 MW, respectively. The carbon-steel Type I HST with the rated volumetric storage density of 23 kg/m^3 and volume of 2 m^3 is adopted for H_2 storage [19]. For low-cost and safe operation, the allowable storage pressure of HST is in the range of 300-500 bar and the standard operation temperature is set to 298 K [20],[30]. The technical specifications of the electrolyzer stack and multi-energy conversion devices are gathered from [20],[24],[31],[40] and listed in Table I. The real-world H_2 demand profile of an HFS located in Shanghai, China is adopted, and the historical traffic data of roadway links in the transportation network are extracted from Gaode Maps for training and validation. The proportion of HVs among all vehicles in the studied region is about 62%. The maximum free-flow velocity and critical traffic density of each roadway link are set to 70 km/h and 10 vehicles/km, respectively [34]. The state-of-the-art forecasting methods in [41],[42] are used for the prediction of wind and solar generations. The real-time electricity price is obtained from [37], and the H_2 price usually has a fixed value in practice, i.e., 12 \$/kg [1]. The H_2 dispersing rate for each HV is set to be 3 kg/min [32]. The rolling horizon optimization of multi-energy conversions and storages for H_2 production is executed over a 24-hour horizon, and the lengths of time slots in the upper and lower layers are set to 15 minutes and 5 minutes, respectively [37].

TABLE I
Technical Specifications of HFS Devices

Electrolyzer stack	N_{c}=4000, z=2, A_{c}=0.268 m^2	$M_{\mathrm{H_2}}$=2 g/mol, F=96485 C/mol
	a_1=50, a_2=2.5	a_3=8.05×10^{-3} Ω·m^2
	a_4=-2.5*10^{-5} Ω·m^2·K	b_1=-1.002 m^2/A, b_2=8.424 m^2·K
	b_3=247.3 m^2·K^2, b_4=1	b_5=0.0085, σ=0.185 V
	ΔG_{bio}=2.894*10^4 J/mol	ΔS_{bio}=16.402 J/(K·mol)
	T_{ref}=298 K, $Q_{\mathrm{H_2}}$=1.4*10^8 J/kg	H_{ref}=1 atm, H_{elz}=1.476 atm
	C_{c}=625 kJ/K, C_{w}=467 kJ/K	Z_{c}=0.167 K/W, Z_{w}=1.659 K/W
	Z_{o}=2.149 °C/W, $I_{\mathrm{c}}^{\mathrm{ra}}$=536 A	R=8.314 J/(K·mol), $I_{\mathrm{c,lim}}$=804 A
	Co_{c}=300 \$, ϑ_{c}=2.1×10^5 h	$T_{\mathrm{c,max}}$= 353 K, d_{f}=8.8×10^{-6} \$/A
	d_{su}=3.9×10^{-4} \$/on	d_{sd}=1.9×10^{-4} \$/off
BES	$P_{\mathrm{ch,max}}$=$P_{\mathrm{dis,max}}$=500 kW	η_{ch}=0.93, η_{dis}=0.93
	$SOC_{\mathrm{BES,min}}$=0.2	$SOC_{\mathrm{BES,max}}$=0.9
	Co_{b}=150 \$/kWh, E_{b}=1000 kWh	r_{b}=0.013%, S_{b}=60%

HST	$m_{\mathrm{HST,min}}$=-20 kg/h, η_{cmp}=0.73	$m_{\mathrm{HST,max}}$=20 kg/h, $m^{\mathrm{ra}}_{\mathrm{HST}}$=46 kg
	$SOC_{\mathrm{HST,min}}$=0.2, V_{HST}=2 m^3	$SOC_{\mathrm{HST,max}}$=0.9, T_{HST}=298 K
	$H_{\mathrm{HST,min}}$=300 bar	$H_{\mathrm{HST,max}}$=500 bar
FC	$\eta^{\mathrm{e}}_{\mathrm{FC}}$=0.7, $\eta^{\mathrm{h}}_{\mathrm{FC}}$=0.25	$E_{\mathrm{FC,max}}$=2.5 MW
Boiler	η_{B}= 0.7	$E_{\mathrm{B,max}}$=100 kW

B. *Comparative results and analysis*

Four schemes are performed to investigate the effectiveness and superiority of the proposed methodology: 1) Scheme 1 is the proposed multi-renewable-to-hydrogen production method with the two-layer multi-variable coordinated control strategy in Sections II and III; 2) Scheme 2 performs multi-renewable-to-hydrogen production as in scheme 1, but the electrolysis temperature control and thermal energy feedback from RES outputs for electrolyzer heating are not considered; 3) Scheme 3 adopts the mainstream commercial AEL based P2G in previous literature [8] for on-site H_2 production at HFSs; 4) Scheme 4 uses the H_2 demand forecasting model in [32] where the HV arrival rate, H_2 fueling amount and dispensing rate at HFS follow the specific probability distributions based on the historical statistical data.

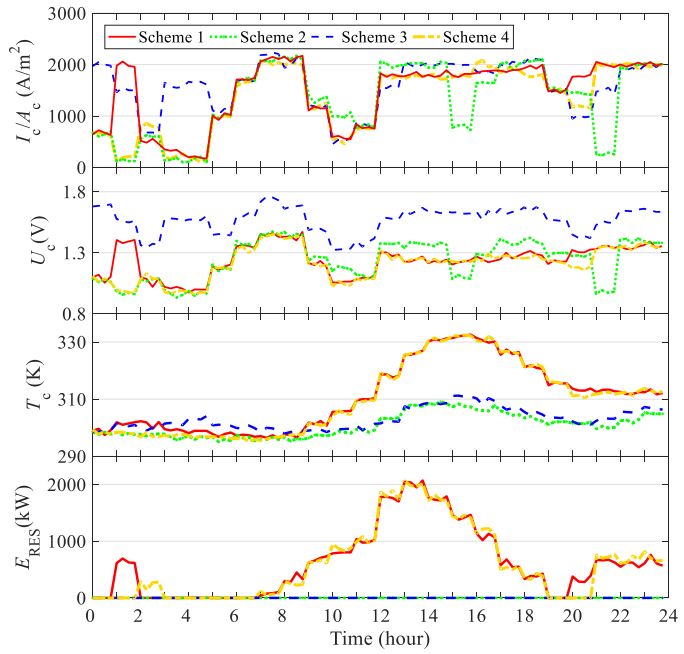

Fig. 7 Operation conditions of electrolyzer with schemes 1-4

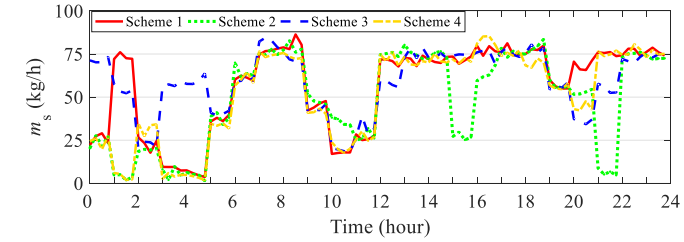

Fig. 8 H_2 production of HFS with schemes 1-4

Fig. 7 depicts the operation conditions of electrolyzer cells, including the controlled electrolysis current, voltage, temperature, and RES energy feedbacks for electrolyzer heating, with schemes 1-4 over a 24-hour horizon. The 24-hour H_2 yield of the HFS is illustrated in Fig. 8. It can be found that schemes 1 and 4 can effectively suppress fluctuations of electrolysis current for H_2 production during hours 7-8 and 12-24 to reduce the electrolyzer degradation cost. Besides, the electrolysis voltage increases with the current and is also affected by the temperature. For example, the electrolysis current of scheme 3 is similar to those of schemes 1 and 4 during hours 17-19 while its voltage is higher due to the lower operation temperature. Essentially, the irreversible losses and Gibbs free energy change of the biomass electrolysis reaction tend to decrease as the reaction temperature is raised, and thus the electrolysis voltage decreases with the increased temperature in schemes 1 and 4. Moreover, it can be observed that the electrolysis voltage in scheme 3 is much larger compared to other schemes because the four-e$^-$ nature of oxygen evolution reaction of water electrolysis requires a higher voltage input than that of the biomass oxidation to afford the same electrolysis current. Additionally, since there is abundant solar irradiation during hours 10-17, a large amount of thermal energy from PVT is harvested to heat up the electrolyzer for H_2 yield rate enhancement in schemes 1 and 4. As wind energy is usually plentiful in the night, the renewable power from WT is primarily used for driving biomass electrolysis during hours 0-2 and 20-24 with schemes 1-4.

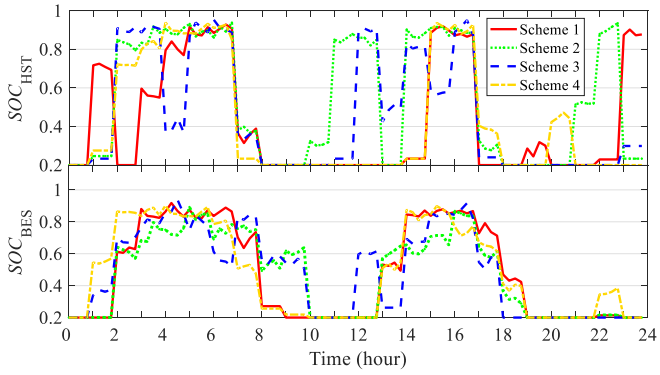

Fig. 9 SOC of HST and BES with schemes 1-4

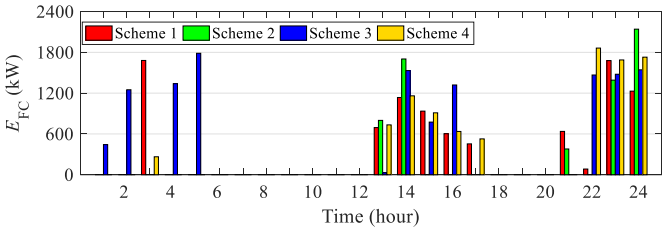

Fig. 10 Power outputs of FC with schemes 1-4

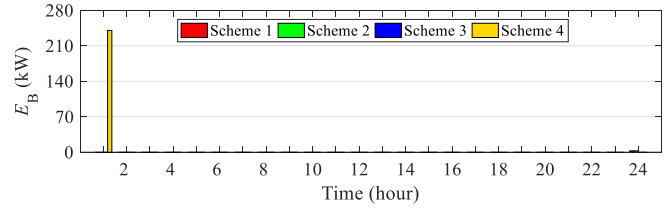

Fig. 11 Thermal energy outputs of electric boiler with schemes 1-4

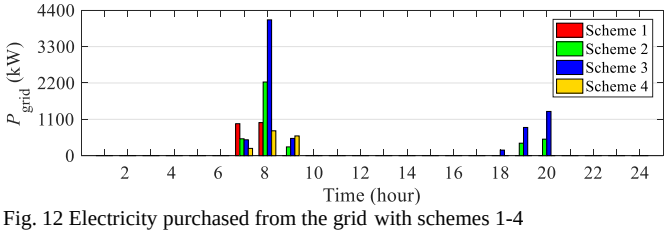

Fig. 12 Electricity purchased from the grid with schemes 1-4

The energy outputs of various storage and conversion devices and the electricity purchased from the grid with schemes 1-4 are depicted in Figs. 9-12. It can be observed that the HST offers a large storage capacity for redundant wind and solar generations, and the charging/discharging actions of BES can provide a certain degree of flexibility for suppressing electrolysis current

fluctuations. Compared with the other schemes, scheme 1 can better coordinate the storage, conversion, and trading of H_2 and electricity to increase the profit of HFS. For instance, as the thermal energy feedback from RESs for electrolyzer heating is not considered in scheme 2, less amount of H_2 is produced and thus the total electricity output from FC for energy arbitrage in the electricity market is less during off-peak H_2 demand hours 13-16 compared to scheme 1, as shown in Fig. 10. Additionally, the boiler outputs are pretty low as shown in Fig. 11, indicating that the conversion of renewable electricity to heating energy and finally to the chemical energy of H_2 is inefficient. Besides, it can be found from Fig. 12 that in schemes 1-4 the extra electricity has to be purchased from the grid to drive biomass electrolysis for H_2 production in hours 7-9 due to insufficient WT and PVT outputs, while the largest amount of electricity is required in scheme 3 because of its low electrolysis efficiency.

TABLE II
COMPARATIVE SYSTEM PERFORMANCE RESULTS OF SCHEMES 1-4

Scheme	1	2	3 (P2G)	4
Total daily profit ($)	**9269.10**	9013.55	8583.79	8999.37
Hydrogen selling revenue ($)	9153.40	9153.40	9153.40	8817.10
Electricity arbitrage ($)	538.76	445.61	24.55	632.67
Electrolyzer degradation cost ($)	304.56	337.22	249.43	313.16
Current fluctuation cost ($)	179.76	212.42	124.63	188.36
BES degradation cost ($)	**118.50**	253.68	337.07	136.47
Total degradation cost ($)	**423.06**	590.90	586.50	449.63
Electrolysis efficiency (%)	**84.64**	75.63	69.29	82.07
MAPE (%)	11.12	11.12	11.12	19.34

The 24-hour system performance results of schemes 1-4 are listed and compared in Table II. It can be found that the current fluctuation cost accounts for a large proportion of the electrolyzer degradation cost, and scheme 1 can effectively suppress the current fluctuation with the most cost-effective control of BES charging/discharging operation. In addition, the contribution of thermal energy harvesting from RESs to the elevated electrolysis temperature in scheme 1 brings about an improvement in electrolysis efficiency by 11.91% and a decrease in current fluctuation cost by 15.38% compared to scheme 2 with single electrolysis current control. Also, compared with the AEL based P2G scheme, scheme 1 can enhance the electrolysis efficiency by 22.15% due to its lower overvoltage and thus less power consumption under the same electrolysis current. Besides, the outcome of the study suggests that the revenue from storing electricity in the form of H_2 for later electricity generation is much smaller than the income from the H_2 market (i.e., supplying HVs). With the CN-based H_2 demand forecasting model, scheme 1 can make more accurate prediction for H_2 loads and obtain more revenue in the H_2 market compared to scheme 4. All in all, it can be concluded that the proposed scheme 1 exhibits superior performance on system economic operation, facilitating the integration and utilization of hybrid RESs for on-site H_2 production at HFSs.

C. Sensitivity analysis

In order to further validate the robustness and superiority of the proposed scheme, schemes 1-4 are performed under different solar generation scenarios varying from 100% to 0% rated capacity of PVT unit. Fig. 13 illustrates the performance results of total daily profit of HFS with schemes 1-4. With the decreasing PVT unit generations, the HFS profit tends to gradually reduce as less amount of renewable electricity can be used to power biomass electrolysis for H_2 production. The comparative results also demonstrate that the proposed scheme 1 can effectively coordinate multi-renewable-to-H_2 production and exhibit superior economic benefits under various RES output scenarios, even in cloudy or rainy weather without solar energy.

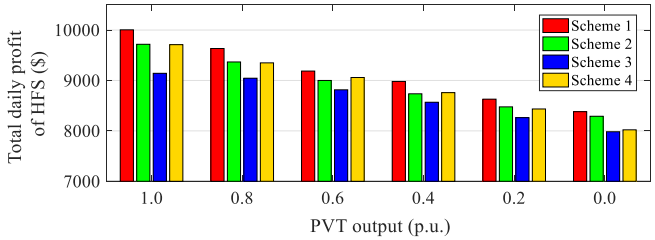

Fig. 13 Effects of different PVT outputs on HFS profit with schemes 1-4

Moreover, in order to investigate the effects of the external environment of electrolyzer stack on the economic performance with the proposed scheme, Fig. 14 shows the results of total daily profit and electricity arbitrage under different ambient air temperatures ranging from 0 ℃ to 35 ℃. It can be observed that with the increase of ambient temperature, both the total daily profit and electricity arbitrage increase. This is because the conductive heat transfer from the electrolyzer to external environment is reduced under high ambient temperatures and more thermal energy can be harvested to accelerate the biomass depolymerization and e- extraction processes. As a result, the H_2 yield is significantly promoted and the surplus H_2 can be stored and opportunistically converted back into electricity by FC to make profit from the electricity market and enhance the total daily profit of HFS.

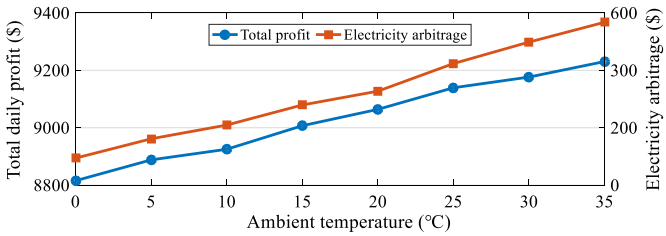

Fig. 14 Effects of ambient temperature on HFS profit

D. Discussion

In order to illustrate the benefits of H_2 load forecasting, the scheme 5 without H_2 load forecasting is performed for comparison, where the historical data of H_2 load at the HFS are used for the operation optimization of multi-renewable-to-H_2 production system. Table III shows the economic performance results of schemes 1 and 5. It can be found that with the proposed CN-based H_2 load forecasting, the daily HFS profit in scheme 1 can be improved by 16.64% compared to scheme 5. This is due to the fact that the H_2 production and storage as well as operational control trajectories of various energy conversion devices are continuously optimized and adjusted based on the updated short-term H_2 load forecasting results in future time horizons to maximize the expected profit. Since the forthcoming H_2 load cannot be estimated in scheme 5, the control decisions on system operation over a finite time horizon are far from optimal and thus less revenue from H_2 sales and more electrolyzer and BES degradation costs are resulted.

On the other hand, the predicted cost of the proposed CN-based H_2 load forecasting model primarily arises from the traffic flow data acquisition. Currently, there are various ways to actively detect real-time traffic flows and count vehicles, such as pneumatic road tube counting, radar microwave sensing, acoustic detection, and video detection, among which video vehicle detection and counting by supervisory cameras is widely used

due to the characteristics of low investment and maintenance cost, long service life, and high accuracy [34]. In addition, as a large number of traffic cameras have already been deployed in the transportation system by local government or private companies, HFSs can pay investors for access to these cameras and thus save the device procurement cost. Hence, video vehicle detection offers a cost-effective way for HFSs to acquire plenty of traffic flow data, and the economic benefits of H_2 load forecasting are much higher than the predicted cost.

TABLE III
COMPARATIVE ECONOMIC PERFORMANCE RESULTS OF SCHEMES 1 AND 5

Scheme	1	5
Total daily profit ($)	**9269.10**	7946.65
Hydrogen selling revenue ($)	**9153.40**	7991.24
Electricity arbitrage ($)	**538.76**	477.22
Electrolyzer degradation cost ($)	**304.56**	320.26
Current fluctuation cost ($)	**179.76**	195.46
BES degradation cost ($)	**118.50**	201.54
Total degradation cost ($)	**423.06**	521.81

V. CONCLUSION

In this paper, a multi-renewable-to-hydrogen production method along with a hierarchical coordinated control strategy is proposed for renewable-dominated HFSs to facilitate the green H_2 yield rate and mitigate the electrolysis current fluctuation caused by RES uncertainties. The following are the key findings of this study: 1) With the coordinated control of electrolysis current, temperature, and charging/discharging of BES for H_2 production, the electrolysis current fluctuation cost is largely reduced and the electrolysis efficiency can be improved by 11.91%; 2) Compared with the mainstream AEL based P2G scheme, the proposed H_2 production method from hybrid RESs can enhance the electrolysis efficiency by 22.15% due to its lower voltage under the same electrolysis current, thus providing a cost-effective renewable-to-hydrogen pathway for HFSs to supply HVs; 3) The revenue from storing electricity in the form of H_2 for later electricity generation and selling is much smaller than the income from selling H_2 directly to HVs. Further on-going research will focus on providing grid ancillary services, such as operating reserves, frequency and voltage regulations, by HFSs in addition to supplying HVs.

REFERENCES

[1] J. Kurtz, M. Peters, and M. Muratori *et al.*, "Renewable hydrogen-economically viable: Integration into the U.S. transportation sector," *IEEE Electrif. Mag.*, vol. 6, no. 1, pp. 8-18, Mar. 2018.

[2] D. Apostolou and G. Xydis, "A literature review on hydrogen refuelling stations and infrastructure. Current status and future prospects," *Renewable Sustain. Energy Rev.*, vol. 113, pp. 1-14, Oct. 2019.

[3] Z. Ding, F. Teng, and P. Sarikprueck *et al.*, "Technical review on advanced approaches for electric vehicle charging demand management, part ii: applications in transportation system coordination and infrastructure planning," *IEEE Trans. Ind. Appl.*, vol. 56, no. 5, pp. 5695-5703 May 2020.

[4] G. Garcia, E. Arriola, and W. Chen *et al.*, "A comprehensive review of hydrogen production from methanol thermochemical conversion for sustainability," *Energy*, vol. 217, pp. 1-17, Feb. 2021.

[5] D. Apostolou, P. Casero, and V. Gil *et al.*, "Integration of a light mobility urban scale hydrogen refuelling station for cycling purposes in the transportation market," *Int. J. Hydrogen Energy*, vol. 46, no. 7, pp. 5756-5762, Jan. 2021.

[6] Z. Zhang, C. Wang, and H. Lv *et al.*, "Day-ahead optimal dispatch for integrated energy system considering power-to-gas and dynamic pipeline networks," *IEEE Trans. Ind. Appl.*, DOI: 10.1109/TIA.2021.3076020, in press, 2021.

[7] D. Gielen, "Hydrogen from renewable power technology outlook for the energy transition," International Renewable Energy Agency, Tech. Rep., Nov. 2018. [Online]. Available: https://www.researchgate.net/publication/328941021

[8] A. Buttler and H. Spliethoff, "Current status of water electrolysis for energy storage, grid balancing and sector coupling via power-to-gas and power-to-liquids: A review," *Renewable Sustain. Energy Rev.*, vol. 82, pp. 2440-2454, Feb. 2018.

[9] S. Joshi and A. Dhoble, "Photovoltaic-Thermal systems (PVT): Technology review and future trends," *Renewable Sustain. Energy Rev.*, vol. 92, pp. 848-882, May 2018.

[10] W. Liu, C. Liu, and P. Gogoi *et al.*, "Overview of biomass conversion to electricity and hydrogen and recent developments in low-temperature electrochemical approaches," *Engineering*, vol. 6, no. 12, pp. 1351-1363, Dec. 2020.

[11] T. Hibino, K. Kobayashi, and M. Ito *et al.*, "Efficient hydrogen production by direct electrolysis of waste biomass at intermediate temperatures," *ACS Sustainable Chem. Eng.*, vol. 6, pp. 9360-9368, May 2018.

[12] W. Liu, Y. Cui, and X. Du *et al.*, "High efficiency hydrogen evolution from native biomass electrolysis," *Energy Environ. Sci.*, vol. 9, pp. 467-472, Mar. 2016.

[13] Z. Dobó and B. Palotás, "Impact of the current fluctuation on the efficiency of alkaline water electrolysis," *Int. J. Hydrog. Energy*, vol. 42, no. 9, pp. 5649-5656, Mar. 2017.

[14] X. Shi, Y. Qian, and S. Yang, "Fluctuation analysis of a complementary wind-solar energy system and integration for large scale hydrogen production," *ACS Sustainable Chem. Eng.*, vol. 8, pp. 7097-7110, Apr. 2020.

[15] N. El-Taweel, H. Khani and H. Farag, "Hydrogen storage optimal scheduling for fuel supply and capacity-based demand response program under dynamic hydrogen pricing," *IEEE Trans. Smart Grid*, vol. 10, no. 4, pp. 4531-4542, July 2019.

[16] H. Khani, N. El-Taweel and H. Farag, "Supervisory scheduling of storage-based hydrogen fueling stations for transportation sector and distributed operating reserve in electricity markets," *IEEE Trans. Ind. Inform.*, vol. 16, no. 3, pp. 1529-1538, Mar. 2020.

[17] L. Chen and J. Shi, "Chemical-assisted hydrogen electrocatalytic evolution reaction (CAHER)," *J. Mater. Chem. A.*, vol. 6, no. 28, pp. 13538-13548, June 2018.

[18] X. Xu, W. Hu, and D. Cao *et al.*, "Optimal operational strategy for an offgrid hybrid hydrogen/electricity refueling station powered by solar photovoltaics," *J. Power Sources*, vol. 451, pp. 1-10, Mar. 2020.

[19] X. Wu, H. Li, and X. Wang, *et al.*, "Cooperative operation for wind turbines and hydrogen fueling stations with on-site hydrogen production," *IEEE Trans. Sustain. Energy*, vol. 11, no. 4, pp. 2775-2789, Oct. 2020.

[20] G. Pan, W. Gu, and Y. Lu *et al.*, "Optimal planning for electricity-hydrogen integrated energy system considering power to hydrogen and heat and seasonal storage," *IEEE Trans. Sustain. Energy*, vol. 11, no. 4, pp. 2662-2676, Oct. 2020.

[21] Y. Gu, Q. Chen, and J. Xue *et al.*, "Comparative techno-economic study of solar energy integrated hydrogen supply pathways for hydrogen refueling stations in China," *Energy Conv. Manag.*, vol. 223, pp. 1-11, Nov. 2020.

[22] Y. Cao, H. Dhahad, and H. Togun *et al.*, "A novel hybrid biomass-solar driven triple combined power cycle integrated with hydrogen production: Multi-objective optimization based on power cost and CO_2 emission," *Energy Conv. Manag.*, vol. 234, pp. 1-14, Feb. 2021.

[23] O. Siddiqui *et al.*, "Development of a novel renewable energy system integrated with biomass gasification combined cycle for cleaner production purposes," *J. Clean Prod.*, vol. 241, pp. 1-21, Dec. 2019.

[24] H. Oh, Y. Choi, and C. Shin *et al.*, "Phosphomolybdic acid as a catalyst for oxidative valorization of biomass and its application as an alternative electron source," *ACS Catal.*, vol. 10, pp. 2060-2068, Jan. 2020.

[25] W. Wu, W. Liu, and W. Mu *et al.*, "Polyoxymetalate liquid-catalyzed polyol fuel cell and the related photoelectrochemical reaction mechanism study," *J. Power Sources*, vol. 318, pp. 86-92, Apr. 2016.

[26] Z. Seh, J. Kibsgaard, and C. Dickens *et al.*, "Combining theory and experiment in electrocatalysis: Insights into materials design," *Science*, vol. 355, pp. 1-12, Jan. 2017.

[27] M. Khan, T. Al-Attas, and N. Yasri *et al.*, "Techno-economic analysis of a solar-powered biomass electrolysis pathway for coproduction of hydrogen and value-added chemicals," *Sustainable Energy & Fuels*, vol. 4, no. 11, pp. 5568-5577, Sep. 2020.

[28] A. Caravaca, W. Garcia-Lorefice, and S. Gil *et al.*, "Towards a sustainable technology for H_2 production: Direct lignin electrolysis in a continuous-flow polymer electrolyte membrane reactor," *Electrochemistry Communications*, vol. 100, pp. 43-47, Jan. 2019.

[29] Y. Zhao, Y. Dong, and Y. Guo *et al.*, "Recent progress of green sorbents-based technologies for low concentration CO_2 capture," *Chinese J. Chem. Eng.*, vol. 31, pp. 113-125, Jan. 2021.

[30] N. Gyawali and Y. Ohsawa, "Integrating fuel cell/electrolyzer/ultracapac-

itor system into a stand-alone microhydro plant," *IEEE Trans. Energy Convers.*, vol. 25, no. 4, pp. 1092-1101, Dec. 2010.

[31] D. Xu, B. Zhou, and Q. Wu *et al.*, "Integrated modelling and enhanced utilization of power-to-ammonia for high renewable penetrated multi-energy systems," *IEEE Trans. Power Syst.*, vol. 35, no. 6, pp. 4769-4780, Nov. 2020.

[32] J. Kurtz, T. Bradley, and E. Winkler *et al.*, "Predicting demand for hydrogen station fueling," *Int. J. Hydrog. Energy*, vol. 45, pp. 32298-32310, Nov. 2020.

[33] X. Ma, H. Zhong, and Y. Li *et al.*, "Forecasting transportation network speed using deep capsule networks with nested LSTM models," *IEEE Trans. Intell. Transp. Syst.*, DOI: 10.1109/TITS.2020.2984813, in press, 2020.

[34] R. Ke, Z. Li, and J. Tang *et al*., "Real-time traffic flow parameter estimation from UAV video based on ensemble classifier and optical flow," *IEEE Trans. Intell. Transp. Syst.*, vol. 20, no. 1, pp. 54-64, Jan. 2019.

[35] Y. Liang, Z. Ding, and T. Ding *et al*., "Mobility-aware charging scheduling for shared on-demand electric vehicle fleet using deep reinforcement learning," *IEEE Trans. Smart Grid*, vol. 12, no. 2, pp.1380-1393, Mar. 2021.

[36] D. Work, S. Blandin, and O. Tossavainen *et al*., "A traffic model for velocity data assimilation," *Applied Mathematics Research eXpress*, vol. 2010, no. 1, pp. 1-35, Apr. 2010.

[37] C. Ju, P. Wang, and L. Goel *et al.*, "A two-layer energy management system for microgrid with hybrid energy storage considering degradation costs," *IEEE Trans. Smart Grid*, vol. 9, no. 6, pp. 6047-6057, Nov. 2018.

[38] C. S. Park, "Fundamentals of engineering economics," Upper Saddle River, NJ, USA: Pearson Education, 2013.

[39] Z. Ding, Y. Lu, and K. Lai *et al.*, "Optimal coordinated operation scheduling for electric vehicle aggregator and charging stations in an integrated electricity-transportation system," *Int. J. Electr. Power Energy Syst.*, vol. 121, pp. 1-11, Oct. 2020.

[40] V. Murty and A. Kumar, "Multi-objective energy management in microgrids with hybrid energy sources and battery energy storage systems," *Prot. Control. Mod. Power Syst.*, vol. 5, no. 1, pp. 1-20, Jan. 2020.

[41] Y.-K. Wu, Y.-C. Wu, and J. Hong *et al.*, "Probabilistic forecast of wind power generation with data processing and numerical weather predictions," *IEEE Trans. Ind. Appl.*, vol. 57, no. 1, pp. 36-45, Jan.-Feb. 2021.

[42] Z. Zhen, S. Pang, and S. Wang *et al.*, "Pattern classification and PSO optimal weights based sky images cloud motion speed calculation method for solar PV power forecasting," *IEEE Trans. Ind. Appl.*, vol. 55, no. 4, pp. 3331-3342, Mar. 2019.